https://doi.org/10.1016/j.jmbbm.2021.104560

Title page

Analytical methods for braided stents design and comparison with FEA

Authors:

Alissa Zaccaria[a,b], Giancarlo Pennati[a], Lorenza Petrini[c].

[a.] LaBS, Dept. of Chemistry, Materials and Chemical Engineering, Politecnico di Milano, Milan, Italy
[b.] Consorzio Intellimech, Bergamo, Italy
[c.] Dept. of Civil and Environmental Engineering, Politecnico di Milano, Milan, Italy

Authors e-mail:

alissa.zaccaria@mail.polimi.it; alissa.zaccaria@intellimech.it
giancarlo.pennati@polimi.it
lorenza.petrini@polimi.it

CRediT author statement

Alissa Zaccaria: conceptualization; software; validation; data curation; formal analysis; investigation; methodology; writing - original draft; visualization.
Giancarlo Pennati: supervision; resources; writing - review & editing.
Lorenza Petrini: supervision; project administration; writing - review & editing.

Corresponding author:

Prof. Lorenza Petrini, PhD
Department of Civil and Environmental Engineering
Politecnico di Milano
Piazza Leonardo da Vinci, 32
20133 Milano (Italy)
tel: +39.02.2399.4307
fax: +39.02.2399.4286
E-mail: lorenza.petrini@polimi.it

Abstract

Braiding technology is nowadays commonly adopted to build stent-like devices. Indeed, these endoprostheses, thanks to their typical great flexibility and kinking resistance, find several applications in mini-invasive treatments, involving but not limiting to the cardiovascular field. The design process usually involves many efforts and long trial and error processes before identifying the best combination of manufacturing parameters. This paper aims to provide analytical tools to support the design and optimization phases: the developed equations, based on few geometrical parameters commonly used for describing braided stents and material stiffness, are easily implementable in a worksheet and allow predicting the radial rigidity of braided stents, also involving complex features such as multiple twists and looped ends, and the diameter variation range. Finite element simulations, previously validated with respect to experimental tests, were used as a comparator to prove the reliability of the analytical results. The illustrated tools can assess the impact of each selected parameter modification and are intended to guide the optimal selection of geometrical and mechanical stent proprieties to obtain the desired radial rigidity, deliverability (minimum diameter), and, if forming processes are planned to modify the shape of the stent, the required diameter variations (maximum and minimum diameters).

Keywords

Radial rigidity, self-expandable stent, in-silico modeling, multiple twist, looped end

1. Introduction

Mini-invasive procedures involving implant of stent-like devices are playing an increasingly important role in the treatment of several diseases (White et al., 2016). Cardiovascular prosthesis are nowadays commonly exploited in different anatomical areas: to restore the physiological flow in coronaries (Schmidt and Abbott, 2018), peripheral arteries (Kokkinidis and Armstrong, 2020), or veins (Murphy, 2019); in the presence of aortic aneurysms and dissections (Maeda et al., 2018); as flow diverter to promote thrombus formation in intracranial aneurysms (Cagnazzo et al., 2017); to occlude the atrial septal defect (Yang and Wu, 2018) or the left atrial appendage in patients affected by non-valvular atrial fibrillation (Pacha et al., 2019); to replace the mitral (Flynn et al., 2018) or aortic native valve (Mahmaljy et al., 2020). Moreover, stents are used to treat pathology affecting the esophagus (Vermeulen and Siersema, 2018), urethra (De Grazia et al., 2019) and tracheobronchial conduit (Grewal et al., 2019).

Based on the specific target, the device must comply with multiple contrasting requirements (Chichareon et al., 2019; Watson et al., 2017), including position stability and appropriate radial stiffness, flexibility, and permeability. In general, it should be possible to implant the stent through a mini-invasive procedure involving the crimping of the device, delivery at the region of interest, and deployment. Based on the principle behind the last phase, the stents are subdivided into balloon-expandable and self-expanding (Schmidt and Abbott, 2018). In the former category, the deployment is forced by a pressurized balloon, for the latter one, featuring large recoverable deformations, the expansion is driven by the elastic recoil, resulting in a lower impact on the vessel. Once in-situ, the stent should be flexible to comply with vessel anatomy and movements, should adequately adhere to the wall, and, in case of

stenotic pathologies, should also provide the radial strength needed to restore the physiological flow (Watson et al., 2017).

The design process aims to optimize the geometrical and material parameters providing the best compromise among all the requirements at issue (Bressloff et al., 2016). In-silico simulations have proved to be a valuable support tool during the design stage, investigating the impact of the involved parameters with a significant saving of money and time with respect to a similar experimental procedure (Kumar et al., 2019), providing additional levels of detail, and expanding the analyses to scenarios resembling in-vivo conditions (Karanasiou et al., 2017; Morlacchi and Migliavacca, 2013; Roy et al., 2012). However, concerning innovative design, the efforts needed to implement and validate the numerical model may not be negligible, and the analyses of each variable impact may be quite expensive. In this light, the advantage deriving from applying simplified analytical models at an early development stage, aiming to identify a suitable range of variation for each parameter, becomes evident.

This work focuses on braided stents, self-expandable endoprosthesis consisting of interlaced wires, and featuring great flexibility and kinking resistance, which make them suitable for several applications (Bishu and Armstrong, 2015; Cremonesi et al., 2015; Madhkour et al., 2019; Seigerman et al., 2019; Subramaniam et al., 2019). The numerical or experimental studies available in the literature on braided stent behavior are very few and very recent (Zaccaria et al., 2020a, Shanahan et al., 2017, McKenna and Vaughan, 2020, McKenna and Vaughan, 2021). In this context, the prediction of mechanical properties through analytical models is not trivial. Jedwab and Clerc (1993) illustrated how to evaluate the longitudinal and radial properties of a cylindrical basic braided structure and validated the results with respect to experimental tests. Moreover, the equations proposed were subsequently used as a

comparator to validate finite element simulations (Shanahan et al., 2017). However, so far, no indications have been presented to predict the radial strength when more complicated features are introduced, like multiple twists and looped ends (Fig. 1a). Moreover, a crucial aspect in the design of braided stents is the definition of the diameter variation range given the initial configuration. On one side, the minimum diameter that can be reached during crimping impacts the device's deliverability. On the other side, complex shapes are usually obtained by deforming an original cylindrical braided texture. Thus, a priori knowledge of the diameter variation range enables estimating (on the basis of predefined geometrical parameters) if a specific configuration is achievable, reducing the trial-and-error efforts.

In this paper, approximated analytical formulae for the prediction of the radial strength of different braided structures are presented and compared with a numerical model validated in a previous work (Zaccaria et al., 2020a). Moreover, equations based on the braided geometrical parameters to obtain the minimum and maximum diameter are illustrated and validated comparing with numerical simulations on a repetitive braided unit.

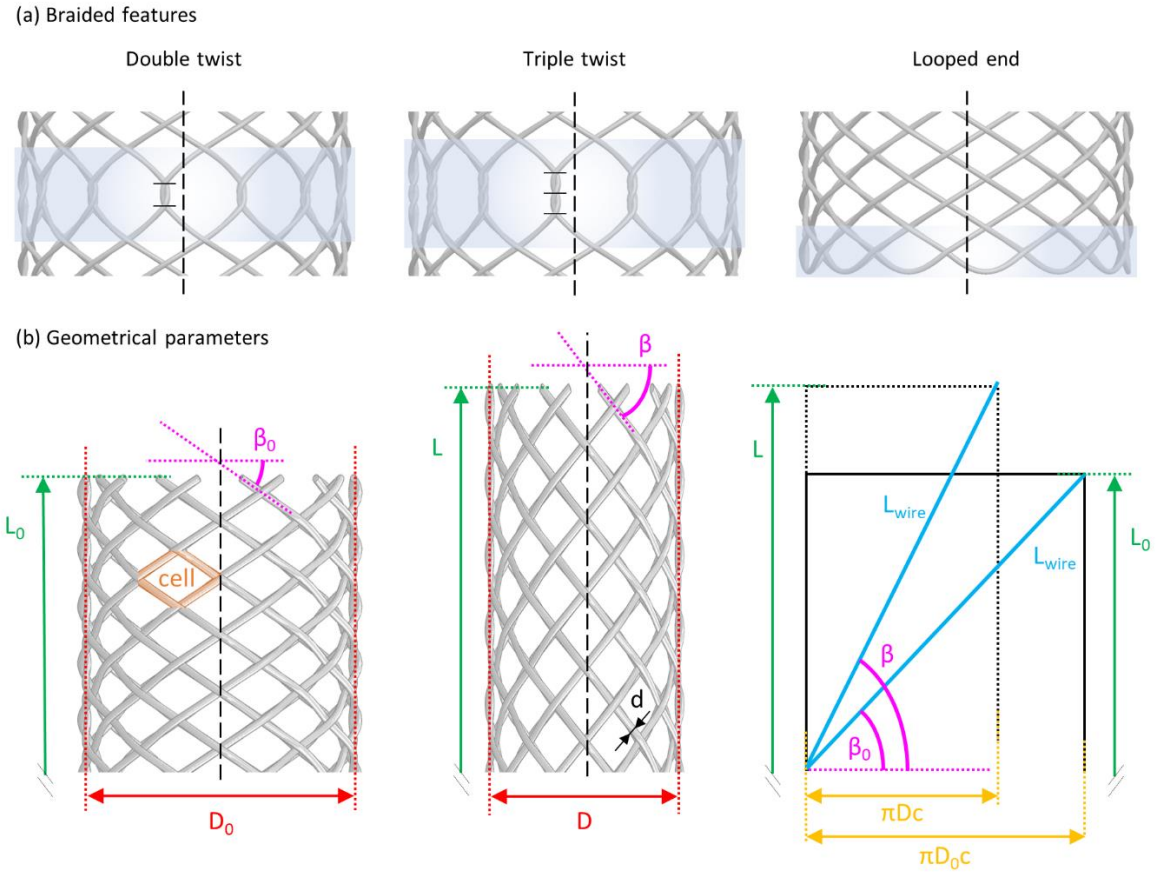

Fig. 1. (a) braided features exemplification: multiple twist (double and triple), looped end. (b) braided geometrical parameters: average stent diameter (D), stent length (L), pitch angle (β), wire diameter (d). The initial values are marked with the subscript '0'. The stent longitudinal axis is indicated by the dashed line. On the right, the single unwound wire is represented in cyan (constant length = L_{wire}) to clarify the relationships among the geometrical parameters.

2. Materials and methods

In the following paragraphs, the analytical formulae developed to predict the radial rigidity of a braided stent are outlined, as well as the equations to derive the minimum and maximum diameter. Finally, the finite element models used as comparators and the numerical analyses performed for validation purposes are presented.

2.1. RADIAL PRESSURE

2.1.1. Cylindrical braided stent

First, the formulae proposed by Jedwab and Clerc (1993) are summarized. These equations allow for calculating longitudinal and radial properties of a cylindrical braided stent, providing the material elastic modulus (E) and Poisson coefficient (ν), and the following geometrical parameters (Fig. 1b):

- single wire diameter (d);
- initial average stent diameter (D_0): easily obtainable by summing 2d to the initial internal diameter, defined by the mandrel used during the braiding procedure;
- initial pitch/braid angle (β_0): defining, in this study, the slope of the wires with respect to the circumferential axis;
- initial length (L_0): longitudinal stent length;
- total number of wires (N): involving both clock-wise and counter clock-wise wires.

Given these values, the initial pitch and the number of coils can be calculated as:

$$p_0 = \pi D_0 \tan(\beta_0) \quad (1)$$

$$c = L_0 / p_0 \quad (2)$$

Assuming that the wire length (L_{wire}) remains constant, and so the sides length of the braided cells (Fig. 1b), and that the wire rotation around the longitudinal axis is prevented by wires intertwining, the deformed stent diameter and length (D, L) are related to the pitch angle (β) through the following equations (Fig. 1b):

$$D = \frac{D_0 \cos(\beta)}{\cos(\beta_0)} \tag{3}$$

$$L = \frac{L_0 \sin(\beta)}{\sin(\beta_0)} \tag{4}$$

Thus, a longitudinal elongation is necessarily associated with a diameter reduction, and it is possible to obtain the same deformed configuration applying a longitudinal force or radial pressure. Considering the stent undergoing a tension test and focusing on the single wire, it is possible to represent it as a helical spring with fixed ends (Fig. 2a) subject to a longitudinal force (F_{wire}) and a moment (M_{wire}), preventing the rotation around the longitudinal axis. Thus, the bending and twisting moments on the wire (m_B, m_T) are calculated as:

$$m_B = M_{wire} \cos(\beta) - F_{wire} R \sin(\beta) \tag{5}$$

$$m_T = M_{wire} \sin(\beta) + F_{wire} R \cos(\beta) \tag{6}$$

Where R is the average radius of the stent (D/2). Moreover, it is possible to connect the bending and twisting moment to the change in curvature (Δκ) and the twist (Δθ) of the wire.

$$\frac{m_B}{EI} = \Delta\kappa = \frac{\cos^2(\beta)}{R} - \frac{\cos^2(\beta_0)}{R_0} \tag{7}$$

$$\frac{m_T}{GI_P} = \Delta\theta = \frac{\cos(\beta)\sin(\beta)}{R} - \frac{\cos(\beta_0)\sin(\beta_0)}{R_0} \tag{8}$$

To obtain the curvature and twist definition reported above, the natural parametrization of the helix $\gamma(t)$ should be considered $\gamma(t) = [R \cdot \cos(t \cdot \cos(\beta)/R)\ ;\ R \cdot \sin(t \cdot \cos(\beta)/R)\ ;\ t \cdot$

$\cos(\beta) \cdot \tan(\beta)]$. Then, the curvature κ is calculated as $\kappa = \|\gamma''(t)\| = \cos^2(\beta)/R$, while the twist θ can be obtained as $\theta = \|b'(t)\|$ where $b(t) = \gamma'(t) \times \gamma''(t)/\|\gamma''(t)\|$.

Thus, the force and moment applied on the wire extremities are related to the pitch angle based on the following equations:

$$F_{wire} = \frac{GI_P\cos(\beta)}{R}\left(\frac{\cos(\beta)\sin(\beta)}{R} - \frac{\cos(\beta_0)\sin(\beta_0)}{R_0}\right) - \frac{EI\sin(\beta)}{R}\left(\frac{\cos^2(\beta)}{R} - \frac{\cos^2(\beta_0)}{R_0}\right) \quad (9)$$

$$M_{wire} = GI_P\sin(\beta)\left(\frac{\cos(\beta)\sin(\beta)}{R} - \frac{\cos(\beta_0)\sin(\beta_0)}{R_0}\right) + EI\cos(\beta)\left(\frac{\cos^2(\beta)}{R} - \frac{\cos^2(\beta_0)}{R_0}\right) \quad (10)$$

In the whole stent, the moment reflects the internal action exerted by the intertwined structure, while the total force $F = F_{wire} \cdot N$ can be represented by substituting the terms involving initial geometrical parameters with three constants:

$$K_1 = \frac{\sin(2\beta_0)}{D_0} \qquad K_2 = \frac{2\cos^2(\beta_0)}{D_0} \qquad K_3 = \frac{D_0}{\cos(\beta_0)} \quad (11)$$

$$F = 2N\left[\frac{GI_P}{K_3}\left(\frac{2\sin(\beta)}{K_3} - K_1\right) - \frac{EI \cdot \tan(\beta)}{K_3}\left(\frac{2\cos(\beta)}{K_3} - K_2\right)\right] \quad (12)$$

Where I and Ip are the moment of inertia and the polar moment of inertia, and G is the shear modulus. To extend or compress the stent, the work done by the external force is equal to $dW = F \cdot (L - L_0)$. The same deformation can be obtained applying a radial pressure P over the lateral surface πDL, corresponding to an energy equal to $dW = P \cdot \pi DL \cdot (D - D_0)/2$. Thus, the pressure needed to vary the average stent diameter can be calculated as follows:

$$P = \frac{2F}{\pi DL}\frac{(L - L_0)}{(D - D_0)} \quad (13)$$

And given the relation among length, diameter and pitch angle:

$$P = \frac{2Fc}{DL\tan(\beta)} \tag{14}$$

Or, if the length is unknown, considering the formulae (1,2)

$$P = \frac{2F}{\pi D^2 \tan^2(\beta)} \tag{15}$$

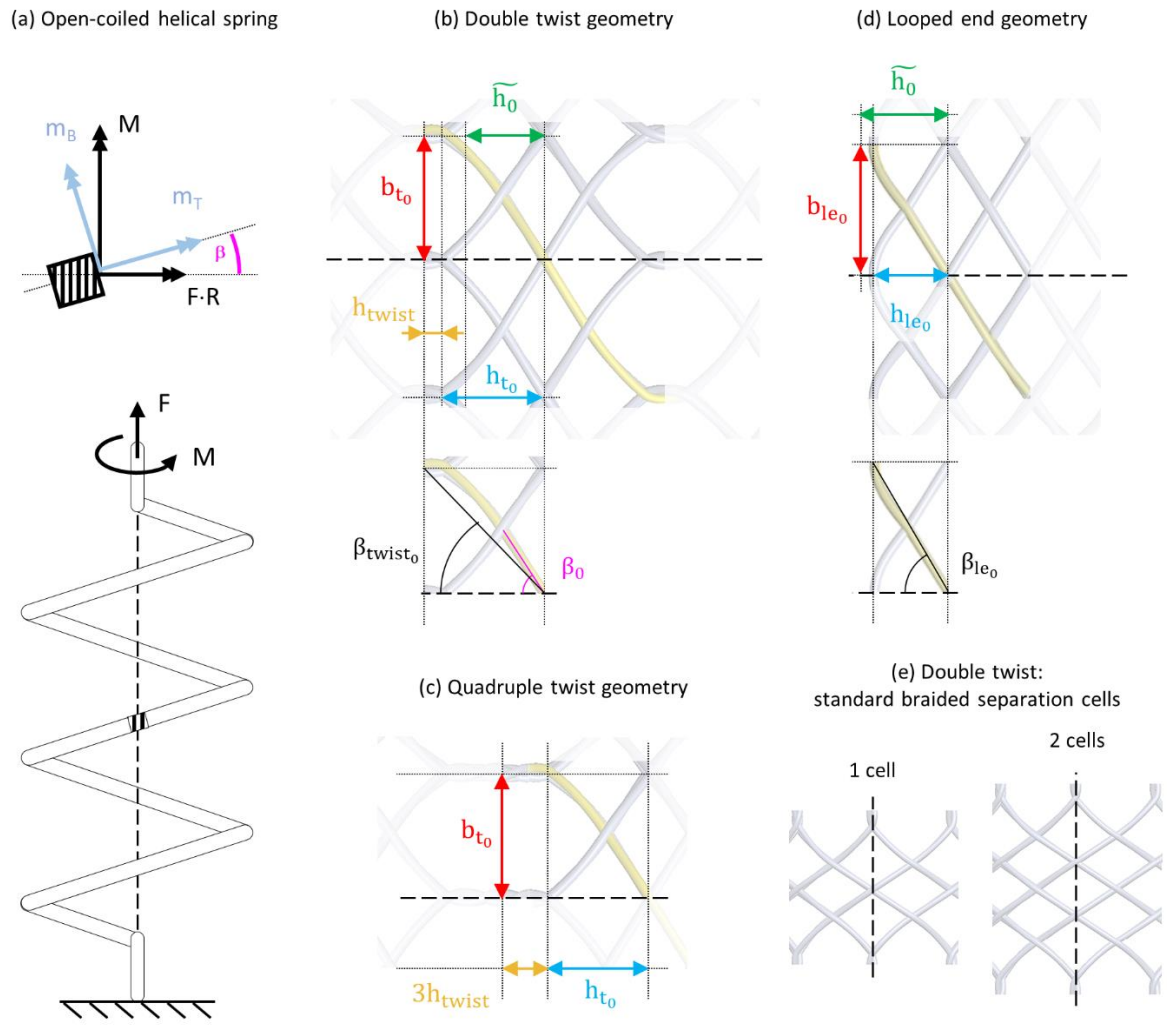

Fig. 2. (a) Open-coiled helical spring with end fixed against rotation: external load and corresponding internal actions acting on a generic element along the helical spring. (b) Double twist geometrical parameters: standard braided length ($\widetilde{h_0}$), twist length (h_{twist}), twisted cell length (h_{t_0}), circumferential dimension (b_{t_0}) and twist pitch angle (β_{twist_0}). (c) Quadruple twist geometrical parameters: twist length ($3h_{twist}$), twisted cell length (h_{t_0}), circumferential dimension (b_{t_0}). (d) Looped end geometrical parameters: length (h_{le_0}), circumferential dimension (b_{le_0}) and looped end pitch angle (β_{le_0}). (e) Double twist: comparison between 1 and 2 standard braided cells between adjacent multiple twist layers.

2.1.2. Double twist

The double twist geometry is illustrated in Fig. 1a and 2b and is obtained by inverting once the braiding direction. The geometrical parameters defining this feature are: b_{t_0}, h_{t_0}, h_{twist} and β_{twist_0}. While the first variable is directly deducible from the braiding parameters as $b_{t_0} = 2\frac{\pi D_0}{N}$, the value h_{t_0} was measured on real devices. In the specific case, this entity was observed to be related to the length of a standard braided texture as $h_{t_0} = 1.24\,\widetilde{h_0} = 1.24\,b_{t_0}\tan(\beta_0)$ (Fig. 2b). Similarly, h_{twist} was measured, and, in the specific case, this entity was observed to be related to the wire diameter as $h_{twist} = 1.84\,d$ (Fig. 2b). Finally, β_{twist_0} was evaluated starting from the previous parameters as $\beta_{twist_0} = \arccos\left(b_{t_0}/L_{dt}\right)$ where $L_{dt} = \sqrt{{b_{t_0}}^2 + (h_{t_0} + h_{twist})^2}$.

During the crimping, the pitch angle should change according to the formula (3). However, at the double twists, the wires are not free to rotate (Fig. 3a). It is possible to compare this segment, involving two crossing points, to a beam subject to a concentrated load whose length is approximated with L_{dt}. Then, the load can be evaluated assuming that the pitch angle variation in correspondence of the extremity (red dot in Fig. 3a) should equalize to the standard braided texture ($\beta - \beta_0$). For the displacement, no conditions were imposed since the double twist wires can separate and, thus, the length of the cell sides (Fig. 1b) is not required to remain constant. Thus, given a diameter variation, it is possible to deduce the deformed pitch angle (β) from Eq. (3) and, based on the linear theory of elasticity (Fig. 3d), the concentrated force acting perpendicular on the wire extremity can be calculated as:

$$F_{wire} = \frac{(\beta - \beta_0) \cdot 2EI}{L_{dt}^2} \tag{16}$$

The total force acting on the stent in the longitudinal direction should be equal to

$$F = \frac{NF_{wire}}{\cos(\beta)} \tag{17}$$

and, starting from the energy equivalence presented by Jedwab and Clerc (1993), Eq. (13), the average radial pressure can be calculated as follows.

$$P = \frac{2F}{\pi D h_{dt}} \cdot \frac{h_{dt} - (h_{t_0} + h_{twist})}{D - D_0} \tag{18}$$

Where h_{dt} can be deduced based on the linear theory of elasticity (Fig. 3d, $\Delta l = h_{dt} - (h_{t_0} + h_{twist})$) as a projection of the displacement connected with the angle variation.

$$h_{dt} = (h_{t_0} + h_{twist}) + \frac{2}{3} L_{dt}(\beta - \beta_0)\cos(\beta_{twist}) \tag{19}$$

Note that the displacement was projected with respect to the twist angle (Fig. 2b) evaluated as

$$\beta_{twist} = \beta_{twist_0} + (\beta - \beta_0) \tag{20}$$

2.1.3. Triple/Quadruple twist

The same logic could be applied to more complex geometries involving additional crossings. Note that the triple twist (Fig. 1a) does not allow to increase the radial rigidity of the standard braided stent since its design does not oppose the wire's rotation due to radial compression, allowing the pitch angle variation (Fig. 3b.1). Concerning the quadruple twist, the geometrical parameters considered are the same: b_{t_0}, h_{t_0}, h_{twist} and β_{twist_0} (Fig. 2c). However, the deformable length is calculated as $L_{qt} = \sqrt{{b_{t_0}}^2 + (h_{t_0} + 3h_{twist})^2}$. The rationale is similar to the previous case, except for the condition imposed on the cantilevered beam extremity. Indeed, in this case, the wires are not free to separate (Fig. 3b.2), and the sides of the cells preserve their original length. Thus, besides the pitch angle, the displacement should also

comply with the geometry constraints. It is possible to assume the beam subject to a concentrated moment and force (Fig. 3b) and, through the superposition principle, deduce their value by imposing at the wire extremity the angle variation, equal to $(\beta - \beta_0)$, and the displacement obtained considering the twist hindrance. Indeed, at a given diameter D, while the circumferential dimension for a standard braided cell is equal to $2\pi D/N$, for the multiple twist geometry, the same dimension would vary according to the formula:

$$b_{qt} = b_{t_0} \frac{\cos(\beta_{twist})}{\cos(\beta_{twist_0})} \tag{21}$$

Where β_{twist} is calculated as in Eq. (20), with β depending on the current D value (Eq. (3)). Thus, the displacement of the extremities was calculated based on the difference between the circumferential dimension calculated through Eq. (21) and the braided texture constraint.

$$F_{wire} = \frac{6EI}{L_{qt}^3}\left(\frac{2}{\sin(\beta_{twist})}\left(b_{qt} - \frac{2\pi}{N}D\right) + L_{qt}(\beta - \beta_0)\right) \tag{22}$$

$$M_{wire} = \frac{EI}{L_{qt}}(\beta - \beta_0) + \frac{1}{2}F_{wire}L_{qt} \tag{23}$$

The boundary conditions were applied in the second overlapping point, corresponding to a length estimated with L_{qt}, assuming that the wires may be able to slightly adjust their position in the correspondence of the first intersection (Fig. 3b.2):

The total force acting on the stent in the longitudinal direction is obtained as previously based on Eq. (17), and the average radial pressure may be calculated as:

$$P = \frac{2F}{\pi D\left(h_{qt} + 2h_{twist}\right)} \cdot \frac{h_{qt} - \left((h_{t_0} + h_{twist})\frac{\sin(\beta_{twist})}{\sin(\beta_{twist_0})}\right)}{D - D_0} \tag{24}$$

h_{qt} can be deduced projecting the displacement imposed at the wire extremity and summing the elongation derived from the rotation in the cylindrical plane. Note that the length

variation in the second factor was calculated with respect to the length resulting from the rigid rotation in the cylindrical plane.

$$h_{qt} = (h_{t_0} + h_{twist})\frac{\sin(\beta_{twist})}{\sin(\beta_{twist_0})} + \frac{1}{\tan(\beta_{twist})}\left(b_{qt} - \frac{2\pi}{N}D\right) \quad (25)$$

2.1.4. Multiple twist: two separation layers

While in the previous sections only one layer of standard braided cells was assumed to separate the subsequent multiple twists, this section aims to extend the formulae to stent designs featuring an additional separation layer (Fig. 2e). In this case, the twist is assumed to behave as previously, considering the same geometrical parameters, while the surface on which the average pressure is evaluated is modified by including the length of the additional braided layer ($(\pi D/N)\tan(\beta)(\sin(\beta) / \sin(\beta_0))$). Thus, only the Eq. (18,24) were adjusted as follows:

$$P = \frac{2F}{\pi D\left(h_{dt} + \frac{\pi D}{N}\tan(\beta)\frac{\sin(\beta)}{\sin(\beta_0)}\right)} \cdot \frac{h_{dt} - h_{dt_0}}{D - D_0} \quad (26)$$

$$P = \frac{2F}{\pi D\left(h_{qt} + 2h_{twist} + \frac{\pi D}{N}\tan(\beta)\frac{\sin(\beta)}{\sin(\beta_0)}\right)} \cdot \frac{h_{qt} - \left(h_{qt_0}\frac{\sin(\beta_{twist})}{\sin(\beta_{twist_0})}\right)}{D - D_0} \quad (27)$$

2.1.5. Looped end

The looped end geometry is illustrated in Fig. 1a and 2c. The geometrical parameters defining this feature are: b_{le_0}, h_{le_0} and β_{le_0}. As previously, the first variable was calculated as $b_{le_0} = 2\pi D_0/N$, while h_{le_0} was measured on real devices. In the specific case, this entity was observed to be related to the length of a standard braided texture as $h_{le_0} = 0.714\,\widetilde{h_0} = 0.714\,b_{le_0}\tan(\beta_0)$ (Fig. 2c). Finally, β_{le_0} was evaluated starting from the previous parameters as $\beta_{le_0} = \arccos\left(b_{le_0}/L_{le}\right)$ where $L_{le} = \sqrt{{b_{le_0}}^2 + {h_{le_0}}^2}$.

Like the quadruple twist feature, the looped end was approximated with a beam subject to a concentrated moment and force, since the boundary conditions involve both angle variation and displacement (Fig. 3c). As previously, the beam was assumed to cover two overlapping points (Fig. 3c), corresponding to the deformable length L_{le}. The angle variation at its extremity is equal to $(\beta - \beta_0)$. Concerning the displacement, the same process applied for the quadruple twist was followed. First, the pitch angle characteristic of the looped end beam, β_{le_0}, was calculated. As previously, the circumferential dimension due to the pitch angle variation would vary according to the formula:

$$b_{le} = b_{le_0}\frac{\cos(\beta_{le})}{\cos(\beta_{le_0})} \tag{28}$$

With $\beta_{le} = \beta_{le_0} + (\beta - \beta_0)$. Thus, the force and moment acting at the extremity was calculated as:

$$F_{wire} = \frac{6EI}{L_{le}^3}\left(\frac{2}{\sin(\beta_{le})}\left(b_{le} - \frac{2\pi}{N}D\right) + L_{le}(\beta - \beta_0)\right) \tag{29}$$

$$M_{wire} = \frac{EI}{L_{le}}(\beta - \beta_0) + \frac{1}{2}F_{wire}L_{le} \tag{30}$$

It can be observed that a lower looped end length ($\downarrow h_{le_0}$) corresponds to a lower looped end pitch angle ($\downarrow \beta_{le_0}$) and a higher circumferential dimension following the same rigid rotation ($\uparrow b_{le}$ at the same β), requiring higher displacement and force ($\uparrow F_{wire}$) to comply with the geometry restriction.

As previously the total longitudinal force (F) is calculated through Eq. (17) and, finally, the radial pressure can be obtained as:

$$P = \frac{2F}{\pi D\left(h_{le} + 2\frac{\pi D}{N}\tan(\beta)\frac{\sin(\beta)}{\sin(\beta_0)}\right)} \cdot \frac{h_{le} - \left(h_{le_0}\frac{\sin(\beta_{le})}{\sin(\beta_{le_0})}\right)}{D - D_0} \tag{31}$$

where:

$$h_{le} = h_{le_0}\frac{\sin(\beta_{le})}{\sin(\beta_{le_0})} + \frac{1}{\tan(\beta_{le})}\left(b_{le} - \frac{2\pi}{N}D\right) \tag{32}$$

The pressure was calculated on a larger surface involving two more crossing layers (Fig. 3c) to facilitate the comparison with the FE model.

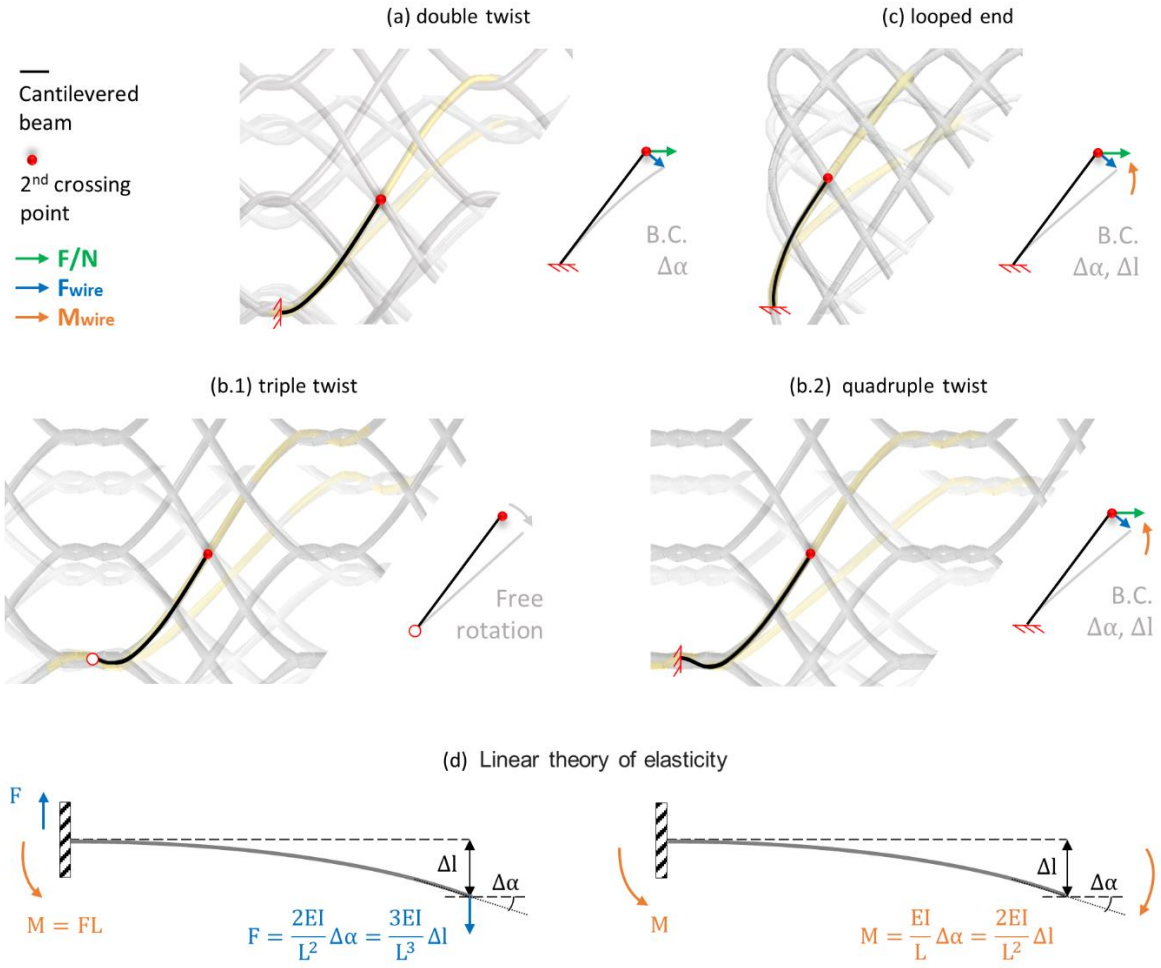

Fig. 3. (a-b-c) Beam approximation for double twist, multiple twists (triple and quadruple) and looped end (black). In yellow the length involved in the radial pressure calculation. (d) Linear theory of elasticity: displacement and rotation for a beam subject to an external concentrated force or a moment.

2.2. MINIMUM AND MAXIMUM DIAMETER

The intertwined structure of the braided allows the wires to rotate and relatively easily adjust their position, elongating or compressing the stent, under external radial loads. However, each device presents a specific limit, both considering crimping and expansion deformations, after which, to further deform it, significant forces would be required. This stiffening is due to the activation of contacts among the wires in points distant from the overlapping area (Fig. 4b). If higher forces are applied, the stent may deform further but never exceed the physical limit defined by the wires' diameter (Fig. 4c).

The pitch angle related to the maximum compressed configuration ($\beta_{\min}$ in Fig. 4c) is obtained assuming that between two crossing points (circumferential distance ≈ πD/N), the longitudinal displacement should be equal to the diameter of the wires.

$$\beta_{\min} = \arctan\left(\frac{dN}{\pi D}\right) \tag{33}$$

As regards the pitch angle at which the first contact among the wires appeared (β_{1c} in Fig. 4b), the intertwined geometry plays the main role. It is possible to assume that the contact occurs on the mean plane (cylindrical surface with diameter equal to the average stent diameter: orange surface in Fig. 4d). The width of the wire footprint on this surface (FP) is determined by the radial coordinate oscillation trend (ΔR) based on the following equation

$$FP = \frac{d}{2}\cos\left(\operatorname{asin}\left(\frac{2\Delta R}{d}\right)\right) \tag{34}$$

Thus, β_{1c} corresponds to the arctangent of FP first derivative with respect to the wire length (l_1/l_2 coordinate in Fig. 4d) at the origin. Considering a sinusoidal intertwining, meaning a radial coordinate oscillation equal to

$$\Delta R = \frac{d}{2}\cos(\theta N) \qquad \theta \in \left[0, \frac{\pi}{N}\right] \tag{35}$$

And observing that the wire length is related to the circumferential coordinate θ through the initial stent diameter and pitch angle

$$l = \theta \frac{D_0}{\cos(\beta_0)} \qquad \theta \in \left[0, \frac{\pi}{N}\right] \tag{36}$$

It is possible to obtain the first derivative of FP with respect to l from Eq. (34,35,36)

$$\frac{\delta FP}{\delta \Delta R} = -\sin\left(\operatorname{asin}\left(\frac{2\Delta R}{d}\right)\right)\frac{1}{\sqrt{1-\left(\frac{2\Delta R}{d}\right)^2}} = -\cos(\theta N)\frac{1}{\sin(\theta N)} \tag{37}$$

$$\frac{\delta \Delta R}{\delta \theta} = -\frac{d}{2} N \sin(\theta N) \tag{38}$$

$$\frac{\delta \theta}{\delta l} = \frac{\cos(\beta_0)}{D_0} \tag{39}$$

$$\frac{\delta FP}{\delta l} = \frac{\delta FP}{\delta \Delta R}\frac{\delta \Delta R}{\delta \theta}\frac{\delta \theta}{\delta l} = dN\frac{\cos(\beta_0)}{2D_0}\cos(\theta N) \tag{40}$$

$$\frac{\delta FP}{\delta l}(l = 0) = dN\frac{\cos(\beta_0)}{2D_0} \tag{41}$$

Thus, β_{1c} is equal to

$$\beta_{1c} = \operatorname{atan}\left(dN\frac{\cos(\beta_0)}{2D_0}\right) \tag{42}$$

Finally, it is possible to obtain the higher and lower diameter at which the first contact is recorded as

$$D_{\min_{1c}} = D_0\frac{\cos(\frac{\pi}{2} - \beta_{1c})}{\cos(\beta_0)} \tag{43}$$

$$D_{\max_{1c}} = D_0\frac{\cos(\beta_{1c})}{\cos(\beta_0)} \tag{44}$$

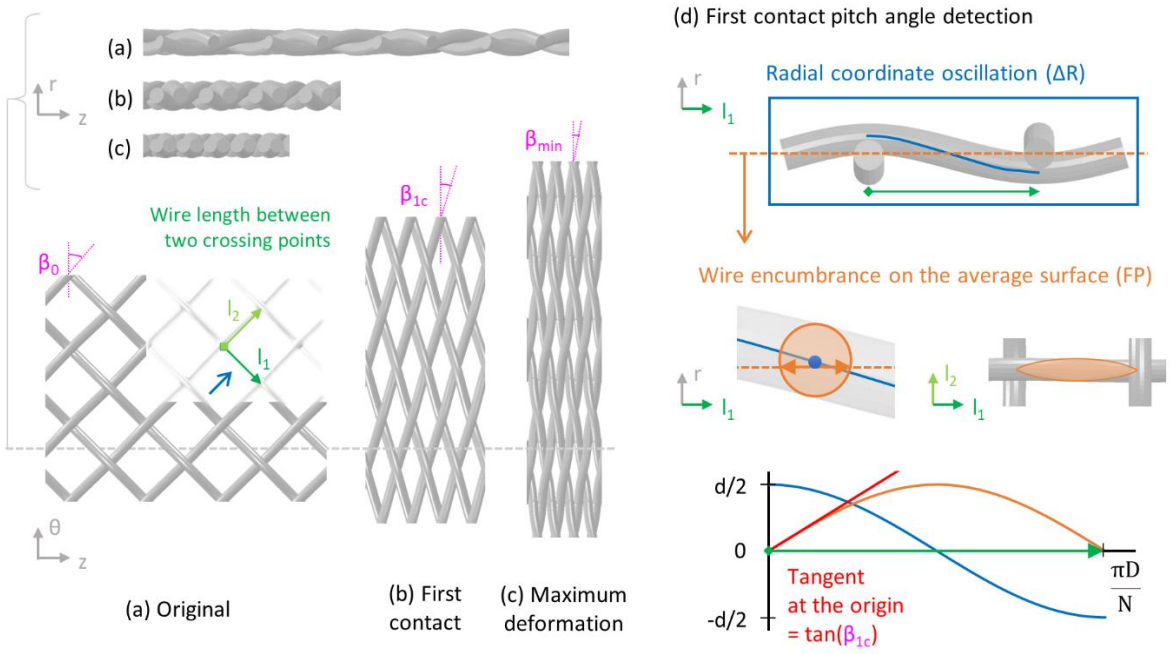

Fig. 4. (a-b-c) Braided texture in the longitudinal-radial plane (zr, top) and in the longitudinal-circumferential plane (zθ, bottom): (a) undeformed configuration; (b) deformation at which the lateral contact among the wires is first recorded; (c) maximum deformation. (d) Detection of the pitch angle corresponding with the first contact deformation (β_{1c}), based on the radial coordinate trend.

2.3. NUMERICAL SIMULATIONS

2.3.1. Radial pressure

The validation was performed comparing the results of the analytical formulae with output of numerical simulations performed in Abaqus/Explicit 2019 (Dassault Systemes Simulia, Providence, RI, USA). Four braided models were built, using 3D parametric equations (Zaccaria et al., 2020b) and starting from the geometrical and material properties of the braided component of the ID Venous System (ID NEST MEDICAL, Strasbourg, FR), named ID Branch, that was deeply analyzed and validated with respect to experimental tests in previous works (Zaccaria et al., 2020a): a cylindrical braided stent, a braided stent with one looped end, the ID Branch design (involving one looped end and five double twist layers), the ID Branch design with triple and quadruple twists instead of double twists.

The standard braided design was compared with the analytical formulae already proposed and validated by Jedwab and Clerc (1993) to assess the finite element model reliability in predicting the average contact pressure on the wall, similar to Shanahan et al. (2017). The remaining were exploited to validate the newly proposed equations. Moreover, the predictions on multiple twists and looped ends were also validated considering design variations: lower stent diameter (internal diameter = 10 mm), variable wire diameter, increased pitch angle (length x1.5), two standard braided cells between multiple twist layers. The comparison was based on crimping simulations in which the stent was surrounded by a cylindrical surface whose diameter is varied to reduce the initial average stent diameter down to 20%. The free open extremity was constrained to stabilize the stent and minimize the boundary effect by preventing the displacement along the circumferential and longitudinal

axis, as well as the rotation around the same axis. Differences due to this constraint are highlighted in the results and discussion sections.

The general contact algorithm was exploited to describe the interaction among the wires (Zaccaria et al., 2020b), imposing a friction coefficient of 0.2 (Kelly et al., 2019; Ma et al., 2012). Concerning the material model, the original stent is made of Nitinol, a super-elastic material whose properties were extracted from experimental tests on wire samples at both 25°C and 37°C (Zaccaria et al., 2020a). However, for the purpose of this study, only the austenite behavior, defining the stress-strain relationship for low deformations, was considered. Indeed, since the interest is to predict the radial pressure on the wall when the stent is fully deployed (≈20% oversizing), it is fair to assume that the local stress remains in the linear elastic region, defined by an elastic modulus of 45000 MPa. In the results and discussion sections, attention was paid to verify the reliability of this approximation.

2.3.2. Minimum and maximum diameter

A repetitive unit involving two crossing points was built to validate the formulae for the maximum and minimum diameter (Fig. 5). Since the equations proposed do not distinguish between a planar or a cylindrical braided structure, the unit was drawn considering both a planar (xyz) and a cylindrical (rϑz) average surface in order to identify potential unpredicted discrepancies. For the planar configuration, the drawing equations (Zaccaria et al., 2020b) were modified as follows:

$$\begin{cases} x(\vartheta) = \dfrac{d}{2} \cdot \cos(\vartheta N) \\ y(\vartheta) = \dfrac{D_0 \vartheta}{2} \\ z(\vartheta) = \dfrac{D_0 \vartheta}{2} \cdot \tan(\alpha) \end{cases} \qquad \text{with } \vartheta \in \left[0, \frac{2\pi}{n}\right] \tag{45}$$

To simulate an elongation and compression deformation, boundary conditions and equation constraints, accounting for the effect of the adjacent hidden braided structure, were introduced at reference points placed in the center of the wires' extremities and rigidly connected with these. Refer to Fig. 5 for the node labels and coordinate systems conventions. For the cylindrical structure, the rotation around the ϑ/z-axis and the translation along the ϑ-axis were prevented. The longitudinal displacement was imposed at nodes 1 and 2, while nodes 5 and 6 were fixed in the same direction. Finally, to account for the repetitive braided texture, the equation constraints have been introduced to ensure that the radial displacement at nodes 1, 2 and 3 is equal to the one at nodes 6, 5 and 4, respectively, and to guarantee the same longitudinal translation at nodes 3 and 4.

For the planar structure, the rotation around the y/z-axis and the translation along the x-axis were prevented. Moreover, nodes 2 and 5 were fixed in the y-direction to avoid unconfined motions. The displacement was imposed at nodes 1 and 2 in the z-direction, while nodes 5

and 6 were fixed in the same direction. Finally, to account for the repetitive braided texture, the equation constraints have been introduced to ensure that the displacement along y at nodes 1 and 3 is equal and opposite to the one recorded at nodes 6 and 4, respectively, and to guarantee the same translation along z at nodes 3 and 4.

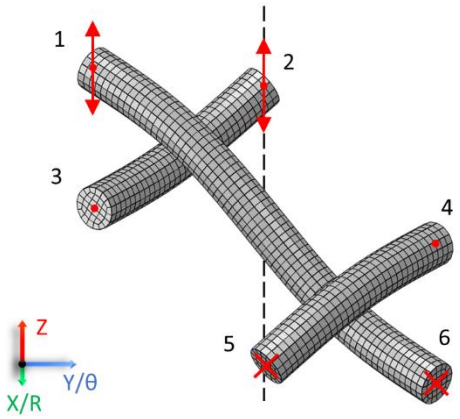

Fig. 5 Numerical boundary conditions to identify the maximum and minimum diameter for a standard braided unit.

3. Results

3.1. RADIAL PRESSURE

3.1.1. Cylindrical braided stent

First, the FE model accuracy in predicting the contact pressure was assessed. More specifically, a crimping simulation on a standard braided texture was performed and compared with the analytical formulae proposed by Jedwab and Clerc (1993) and already validated with respect to experimental tests. The ID Branch geometrical parameters were used: D0= 13.77mm; d= 0.23mm; β0= 32°; N=26 (Fig. 6). The numerical average contact pressure at 20% oversizing differs from the analytical prediction for less than 1.39% in the central portion, proving the reliability of the simulation. Note that the FE model is also able to assess the extremity weakness. Indeed, the average pressure on the last three cells in proximity of the free open end is decreased by 21.95%. Moreover, the length variation in the model is equal to 38.73%, close to the 38.50% variation predicted by the formulae.

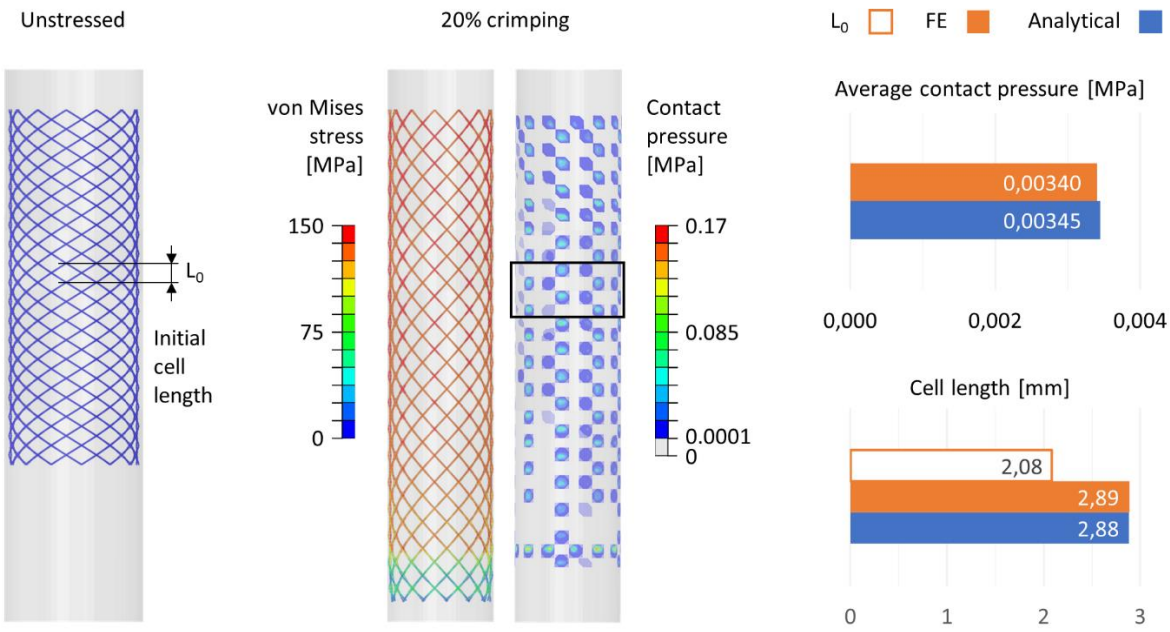

Fig. 6 Crimping of a standard braided sample. From left to right: undeformed configuration; stent deformed configuration with von Mises stress colored map (note that on one end only radial displacement and rotation around the radial axis are allowed); crimping surface with contact pressure colored map; comparison between FE results and analytical prediction in terms of average contact pressure (calculated for the model on the section enclosed by the black rectangle) and cell length. Lo indicate the cell length in the undeformed configuration.

3.1.2. Double twist

Concerning the double twist feature, the ID Branch original design, previously validated through the comparison with experimental tests (Zaccaria et al., 2020a), was used to assess the accuracy of the analytical predictions (Fig. 7 "Double twist"). The geometrical parameters of the braided texture are reported above, while the dimensions defining the double twist geometry are: h_{dt_0}=2.563mm, h_{twist}=0.423mm, b_{dt_0}=3.327mm. The analytical and FE results show differences of 0.94% and 2.44% in terms of contact pressure and deformed length, respectively (Fig. 8 "ID Branch").

To further validate the formulae, some design modifications were investigated. First, the stent diameter was modified keeping the same pitch angle (10 mm internal diameter), and three

different wires diameter were evaluated (0.16/0.17/0.18 mm). Moreover, the pitch angle impact was assessed by scaling the length of the original model by 3/2. The analytical radial pressure and the final length differ from FE results for lower than 3.35% and 2.15%, respectively (Fig. 8 “D0 10.36 mm”, “D0 10.34 mm”, “D0 10.32 mm”, “L0 x 1.5”).

3.1.3. Triple/Quadruple twist

Concerning the triple twist, no significant variations were recorded with respect to the standard braided design (average contact pressure = 0.00322 MPa). For the quadruple twist (Fig. 7 “Quadruple twist”), the formulae proposed correctly predict the contact pressure and the final length of the designs investigated, showing differences with respect to the FE results below 6.2% (Fig. 8). Note that the average contact pressure is close to the double twist results (difference <6.7%).

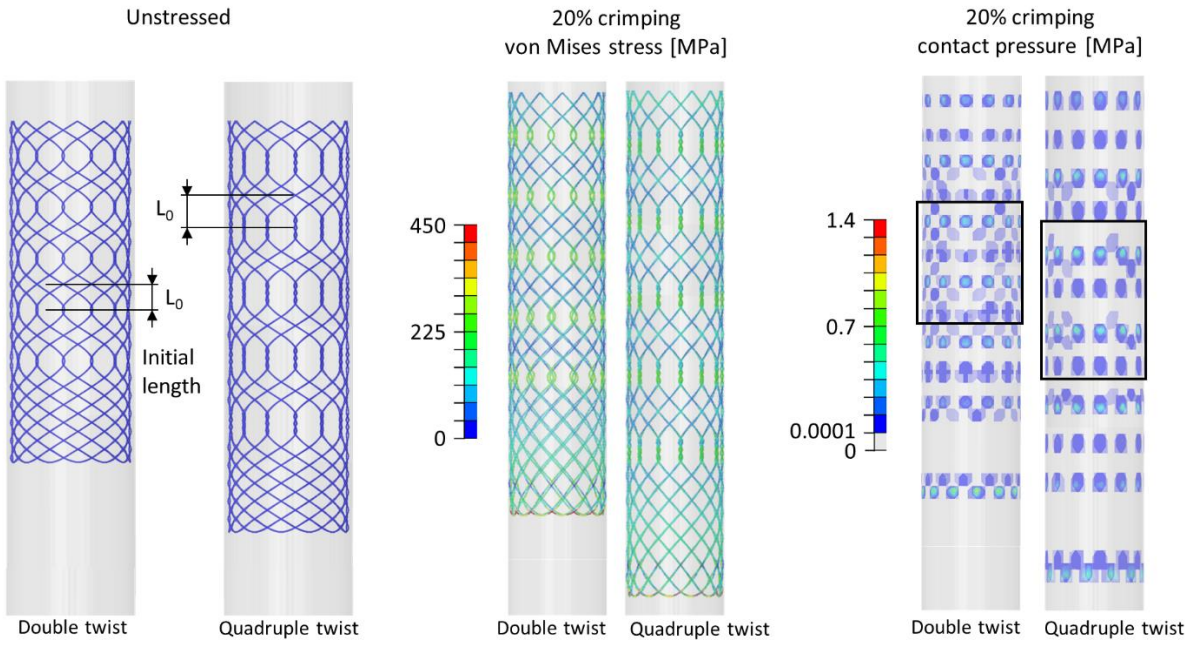

Fig. 7. Crimping of the ID Branch model with double or quadruple twists. From left to right: undeformed configuration; stent deformed configuration with von Mises stress colored map (note that on the open end only radial displacement and rotation around the radial axis are allowed to minimize boundary effects); crimping surface with contact pressure colored map.

3.1.4. Multiple twist: two separation layers

As an additional validation, a second separation layer was introduced between two sequential multiple twist traits (Fig. 2d) and the equations were updated as outlined in the materials and methods section. The analytical formulae reliability is demonstrated by the low difference with respect to the FE model, below 5.1% and 2.9% in terms of radial pressure and elongation (Fig. 8, “2 cells”).

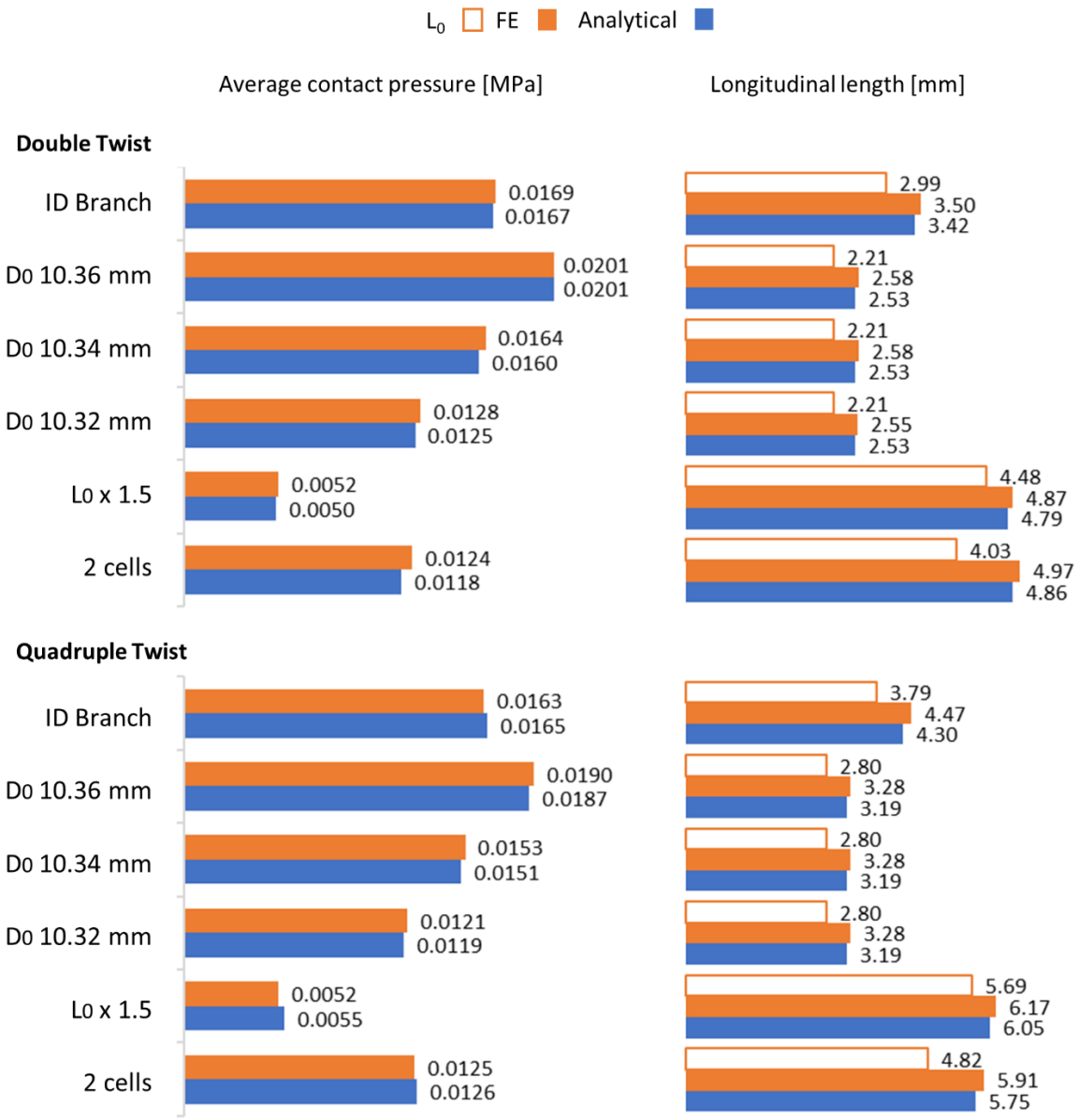

Fig. 8 Comparison for the double and quadruple twist designs between FE results and analytical prediction in terms of average contact pressure (calculated for the model on the sections enclosed by the black rectangles in Fig. 7) and unit length.

3.1.5. Looped end

The Looped end prediction were validated based on the original ID Branch geometrical parameters (Fig. 9 “ID Branch”), the reduced stent diameter design with variable wires diameter (Fig. 9 “D0 10.36 mm”, “D0 10.34 mm”, “D0 10.32 mm”), and the elongated configuration (Fig. 9 “L0 x 1.5”). The differences in terms of average contact pressure and final length do not exceed 6.7%. Note that, in this case, the pressure was evaluated on the last two cell lines (Fig. 9 “Unstressed”).

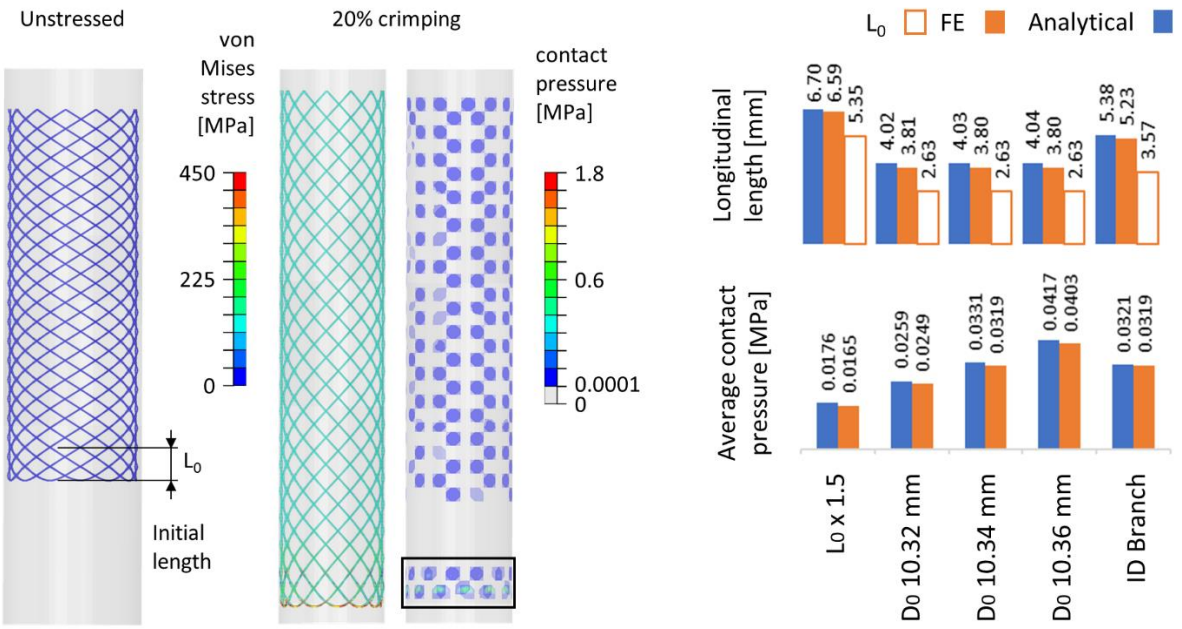

Fig. 9 Crimping of a standard braided sample with a looped end. From left to right: undeformed configuration; stent deformed configuration with von Mises stress colored map (note that on the open end only radial displacement and rotation around the radial axis are allowed); crimping surface with contact pressure colored map; comparison between FE results and analytical prediction in terms of average contact pressure (calculated for the model on the section enclosed by the black rectangle) and cell length.

3.2. MINIMUM AND MAXIMUM DIAMETER

Both a tensile and compression simulation were performed on a planar and cylindrical braided unit involving two crossing points. Generic geometrical parameters were used: D0= 5 mm; d= 0.2 mm; β0= 45°; N=40.

Fig. 10 reports the total longitudinal force-diameter curves. The total longitudinal force was calculated as

$$F_l = \frac{N}{4}((F_{l_1} + F_{l_2}) - (F_{l_5} + F_{l_6})) \quad (46)$$

while the diameter in the planar configuration was calculated as

$$D = D_0 - \frac{N\,\Delta y}{2\pi} \quad (47)$$

where Δy is half of the unit length variation in this direction (Fig. 10b).

Observing the longitudinal force–diameter curves in all the simulations it can be identified a stiffening point, associated with the first contact diameter. The planar and cylindrical configurations differ due to the absence of force in the first case before the first contact appear. However, the point in which the slope variation appear does not vary, proving the reliability of the approximation considered. The first contact points are reported below and were calculated as the mean between the first point associated with a significant force increase and the point before:

- $Dmin_{1c}$ cylindrical = 3.77 ± 0.24 mm;
- $Dmin_{1c}$ planar = 3.77 ± 0.23 mm;
- $Dmax_{1c}$ cylindrical = 13.62 ± 0.02 mm;
- $Dmax_{1c}$ planar = 13.62 ± 0.02 mm.

The prediction based on the formulae proposed are within the identified range: Dmin1c = 3.85 mm and Dmax1c = 13.61 mm.

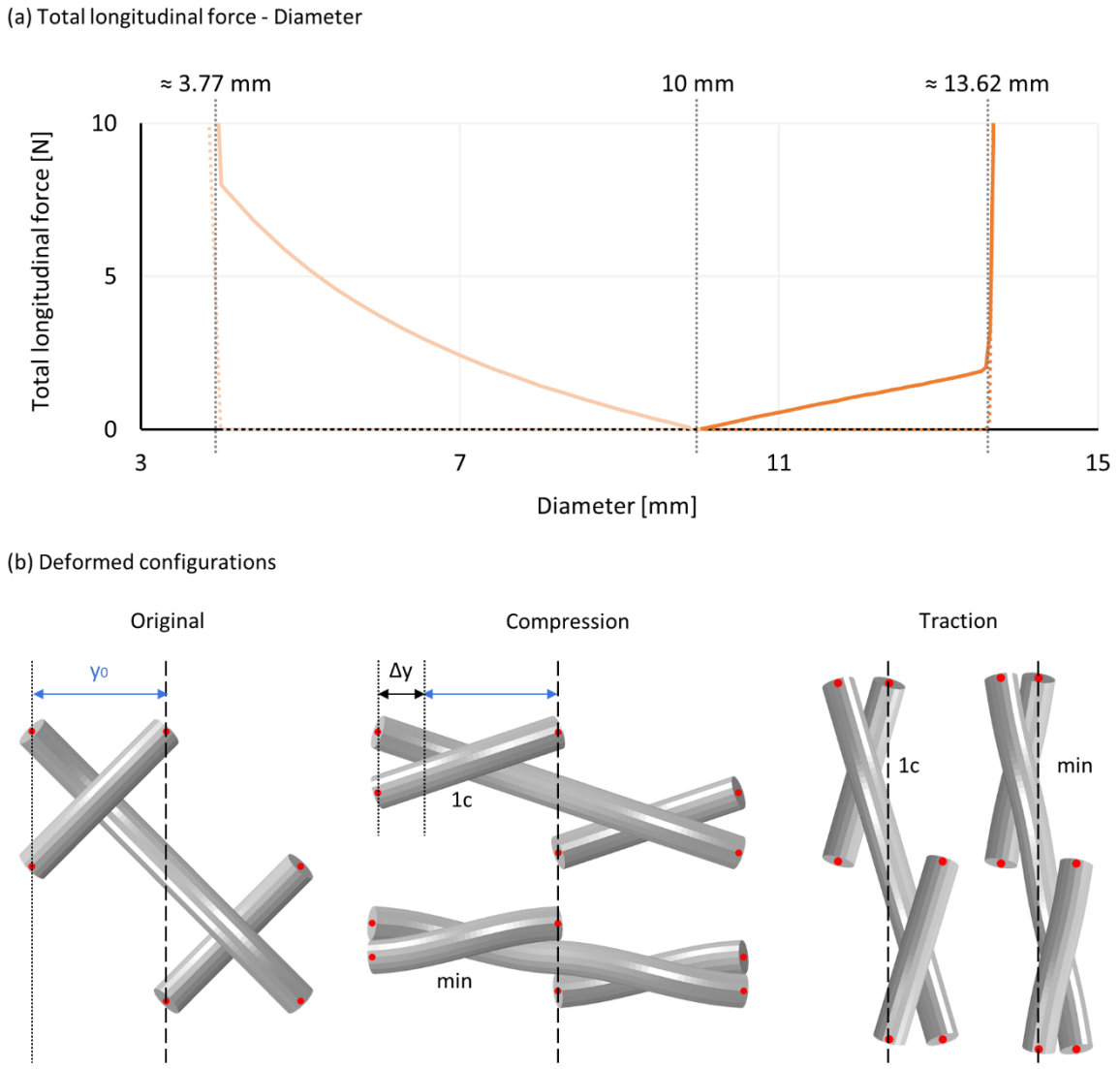

Fig. 10. Maximum and minimum diameter for a standard braided unit: (a) force-diameter curves for a planar and a cylindrical unit undergoing a traction and a compression test; (b) undeformed (left) and deformed configuration under compression (center) and tension (right) for the planar unit at the diameter corresponding with the first contact deformation (1c) and at the maximum compression and traction, and illustration of the Δy term used in Eq. (47). The black dashed lines in (c) indicates the longitudinal axis.

4. Discussion

This work focuses on braided stent design and presents approximated formulae to predict the radial pressure and the diameter variation range.

Jedwab and Clerc (1993) have already outlined and validated with respect to experimental data the equations that allow to connect the longitudinal and the radial deformation and predict the radial stiffness at a given oversizing. These formulae were illustrated in this work and applied to derive the average radial pressure at 20% oversizing for a standard braided stent using as reference the geometrical parameters of the ID Branch (the braided component of the ID Venous System, ID Nest Medica). Then, a FE simulation was performed to assess the numerical model capability in evaluating the contact pressure on the confined wall. Since the errors in terms of average contact pressure and length variation do not exceed 1.4%, the FE model is deemed reliable. Moreover, the simulation highlighted the weakness associated with open ends. In general, the free ends of the wires tend to collapse, decreasing the pressure recorded at this level. Thus, in the subsequent simulations, the open ends were constrained, as outlined in the material and methods section. Indeed, as visible in Fig. 6 for the standard braided model, the boundary effects at the constrained open end are significantly reduced with respect to the free extremity.

Following, the FE simulations were used to validate the analytical predictions concerning multiple twists and looped ends with variable design parameters. Given the comparability of the results both in terms of average radial pressure and length variation, differing for less than 10%, the analytical formulae can be judged trustworthy. Note that, in the diameter variation range considered, the stress distribution within the wires do not exceed 450 MPa, complying with the assumption of linearity for the Nitinol stress-strain relationship.

Nevertheless, this hypothesis would not be valid at higher deformation, for example if the radial pressure on the delivery catheter has to be investigated.

Concerning the multiple twist feature, it could also be interesting to observe the low variation in terms of radial pressure for double and quadruple twists. Indeed, even if the longitudinal force is higher for the quadruple twists, given the displacement constraint, this effect is balanced by the lower axial deformation of the cantilevered beam and the larger surface. Instead, as explained in the materials and methods section, the triple twist does not allow to increase the radial rigidity. Indeed, a similar simulation performed with a triple twist design showed an average radial pressure of 0.00322 MPa, 5.3% lower than the standard braided model result. This is due to the fact that at the triple twist, the wires are able to adjust their position, minimizing the bending and torsion moments that would arise in a standard helicoidal wire due to the curvature variation. For the looped end feature, observing the contact pressure distribution in Fig. 9, it becomes clear the need to evaluate the radial pressure on the last two cells layers instead of considering only the last one. Indeed, the contact pressure is localized in correspondence of the second and third crossing points.

Note that, even if the formulae were presented starting from the ID Branch device geometry (Fig. 2b-c), specifically, on the cylindrical segment of the stent, involving one looped end and five double twist traits separated from each other by one braided layer (Fig. 2d “1 cell”), their extendibility to different design has been demonstrated. The most critical geometrical parameters to be defined are $\mathrm{h}_{\mathrm{dt}_0}/\mathrm{h}_{\mathrm{qt}_0}$, $\mathrm{h}_{\mathrm{twist}}$ and $\mathrm{h}_{\mathrm{le}_0}$. If no data are available, the relations illustrated between these values and the braiding parameters could provide preliminary information. However, as soon as one sample is manufactured, these values should be measured and updated.

Concerning the diameter variation range, the formulae illustrated for a sinusoidal intertwining correctly identify the maximum and minimum diameter at which the first contact among the wires occurs. Further deformations beyond these limits are possible but require a significant compressive or tensile force increase. Note that the planar configuration does not record any force until that point. Indeed, without contacts among the wires, a longitudinal elongation reflects in a rigid rotation, in contrast with the cylindrical configuration where the z-displacement modify the curvature of the beam, generating bending and twisting moments. The values identified are good estimators of the maximum and minimum diameter, the latter of which affect the system deliverability. However, during the braiding procedure, a tensile load is usually applied at the wire extremities, resulting in a more linear trend with respect to the sinusoidal oscillation and, subsequently, in a narrower diameter variation range (↑ β_{1c}, Fig. 4). Thus, the β_{1c} obtained with the sinusoidal approximation may be considered as the lower limit to which the actual device tends with decreasing load applied during the manufacturing. A more accurate result could be obtained by modifying the wire's radial oscillation (ΔR, Fig. 4, Eq. (35)) based on the applied load.

5. Conclusion

In this paper, analytical formulae, based on geometrical and mechanical parameters, have been developed for the prediction of the radial strength of different braided structures and the evaluation of minimum and maximum diameter, obtainable once defined the geometry. The efficacy of the proposed approach has been checked by comparing the analytical results with computational data obtained from a finite element model validated in previous work (Zaccaria et al., 2020a).

The validity of the illustrated model, as a simplistic strategy, is limited. Indeed, non-linearities and manufacturing process specificity are not considered. Nevertheless, it can be deemed a helpful tool for the design and optimization phases, easy to be implemented, and associated with a significant reduction in terms of time and production cost thanks to the possibility to preliminary identify a suitable range for design parameters such as stent diameter, pitch angle, the number of wires and their diameter, as well as material stiffness and the introduction of multiple twists and looped end features.

6. Acknowledgements

The authors acknowledge David Contassot and ID Nest Medical for discussing the issues with the authors and provide useful insights from the ID Branch design point of view.

7. References

Bishu, K., Armstrong, E.J., 2015. Supera self-expanding stents for endovascular treatment of femoropopliteal disease: a review of the clinical evidence. Vasc. Health Risk Manag. 11, 387–395. https://doi.org/10.2147/VHRM.S70229

Bressloff, N.W., Ragkousis, G., Curzen, N., 2016. Design optimisation of coronary artery stent systems. Ann. Biomed. Eng. 44, 357–367. https://doi.org/10.1007/s10439-015-1373-9

Cagnazzo, F., Mantilla, D., Lefevre, P.H., Dargazanli, C., Gascou, G., Costalat, V., 2017. Treatment of middle cerebral artery aneurysms with flow- diverter stents: A systematic review and meta-Analysis. Am. J. Neuroradiol. 38, 2289–2294. https://doi.org/10.3174/ajnr.A5388

Chichareon, P., Katagiri, Y., Asano, T., Takahashi, K., Kogame, N., Modolo, R., Tenekecioglu, E., Chang, C.C., Tomaniak, M., Kukreja, N., Wykrzykowska, J.J., Piek, J.J., Serruys, P.W., Onuma, Y., 2019. Mechanical properties and performances of contemporary drug-eluting stent: focus on the metallic backbone. Expert Rev. Med. Devices 16, 211–228. https://doi.org/10.1080/17434440.2019.1573142

Cremonesi, A., Castriota, F., Secco, G.G., Macdonald, S., Roffi, M., 2015. Carotid artery stenting: An update. Eur. Heart J. 36, 13–21. https://doi.org/10.1093/eurheartj/ehu446

De Grazia, A., Somani, B.K., Soria, F., Carugo, D., Mosayyebi, A., 2019. Latest advancements in ureteral stent technology. Transl. Androl. Urol. 8, S436–S441. https://doi.org/10.21037/tau.2019.08.16

Flynn, C.D., Wilson-Smith, A.R., Yan, T.D., 2018. Novel mitral valve technologies-transcatheter mitral valve implantation: A systematic review. Ann. Cardiothorac. Surg.

7, 716–723. https://doi.org/10.21037/acs.2018.11.01

Grewal, H.S., Dangayach, N.S., Ahmad, U., Ghosh, S., Gildea, T., Mehta, A.C., 2019. Treatment of Tracheobronchial Injuries: A Contemporary Review. Chest 155, 595–604. https://doi.org/10.1016/j.chest.2018.07.018

Jedwab, M.R., Clerc, C.O., 1993. A study of the geometrical and mechanical properties of a self- expanding metallic stent—theory and experiment. J. Appl. Biomater. 4, 77–85.

Karanasiou, G.S., Papafaklis, M.I., Conway, C., Michalis, L.K., Tzafriri, R., Edelman, E.R., Fotiadis, D.I., 2017. Stents: biomechanics, biomaterials, and insights from computational modeling. Ann. Biomed. Eng. 45, 853–872. https://doi.org/10.1007/s10439-017-1806-8

Kelly, N., McGrath, D.J., Sweeney, C.A., Kurtenbach, K., Grogan, J.A., Jockenhoevel, S., O'Brien, B.J., Bruzzi, M., McHugh, P.E., 2019. Comparison of computational modelling techniques for braided stent analysis. Comput. Methods Biomech. Biomed. Engin. 22, 1334–1344. https://doi.org/10.1080/10255842.2019.1663414

Kokkinidis, D.G., Armstrong, E.J., 2020. Current developments in endovascular therapy of peripheral vascular disease. J. Thorac. Dis. 12, 1681–1694. https://doi.org/10.21037/jtd.2019.12.130

Kumar, A., Ahuja, R., Bhati, P., Vashisth, P., Bhatnagar, N., 2019. Design Methodology of a Balloon Expandable Polymeric Stent. J. Biomed. Eng. Med. Devices 04. https://doi.org/10.35248/2475-7586.19.4.139

Ma, D., Dargush, G.F., Natarajan, S.K., Levy, E.I., Siddiqui, A.H., Meng, H., 2012. Computer modeling of deployment and mechanical expansion of neurovascular flow diverter in patient-specific intracranial aneurysms. J. Biomech. 45, 2256–2263.

https://doi.org/10.1016/j.jbiomech.2012.06.013

Madhkour, R., Wahl, A., Praz, F., Meier, B., 2019. Amplatzer patent foramen ovale occluder: safety and efficacy. Expert Rev. Med. Devices 16, 173–182. https://doi.org/10.1080/17434440.2019.1581060

Maeda, K., Ohki, T., Kanaoka, Y., 2018. Endovascular Treatment of Various Aortic Pathologies: Review of the Latest Data and Technologies. Int. J. Angiol. 27, 81–91. https://doi.org/10.1055/s-0038-1645881

Mahmaljy, H., Tawney, A., Young, M., 2020. Transcatheter Aortic Valve Replacement (TAVR / TAVI , Percutaneous Replacement) Contraindications Clinical Signi cance Enhancing Healthcare Team Outcomes 9–12.

McKenna, C. G., Vaughan, T. J., 2020. An experimental evaluation of the mechanics of bare and polymer-covered self-expanding wire braided stents. J. Mech. Behav. Biomed. Mater. 103, 103549. https://doi.org/10.1016/j.jmbbm.2019.103549

McKenna, C. G., Vaughan, T. J., 2021. A finite element investigation on design parameters of bare and polymer-covered self-expanding wire braided stents. J. Mech. Behav. Biomed. Mater. 115, 104305. https://doi.org/10.1016/j.jmbbm.2020.104305

Morlacchi, S., Migliavacca, F., 2013. Modeling stented coronary arteries: where we are, where to go. Ann. Biomed. Eng. 41, 1428–1444. https://doi.org/10.1007/s10439-012-0681-6

Murphy, E., 2019. Surveying the 2019 Venous Stent Landscape. Endovasc. Today 18, 53–64.

Pacha, H.M., Al-khadra, Y., Soud, M., Darmoch, F., Pacha, A.M., Alraies, M.C., 2019. Percutaneous devices for left atrial appendage occlusion: A contemporary review. World J. Cardiol. 11, 57–70. https://doi.org/10.4330/wjc.v11.i2.57

Roy, D., Kauffmann, C., Delorme, S., Lerouge, S., Cloutier, G., Soulez, G., 2012. A literature review of the numerical analysis of abdominal aortic aneurysms treated with endovascular stent grafts. Comput. Math. Methods Med. https://doi.org/10.1155/2012/820389

Schmidt, T., Abbott, J., 2018. Coronary Stents: History, Design, and Construction. J. Clin. Med. 7, 126. https://doi.org/10.3390/jcm7060126

Seigerman, M.E., Nathan, A., Anwaruddin, S., 2019. The Lotus valve system: an in-depth review of the technology. Curr. Cardiol. Rep. 21, 157. https://doi.org/10.1007/s11886-019-1234-5

Shanahan, C., Tiernan, P., Tofail, S.A.M., 2017. Looped ends versus open ends braided stent: A comparison of the mechanical behaviour using analytical and numerical methods. J. Mech. Behav. Biomed. Mater. 75, 581–591. https://doi.org/10.1016/j.jmbbm.2017.08.025

Subramaniam, K., Ibarra, A., Boisen, M.L., 2019. Echocardiographic Guidance of AMPLATZER Amulet Left Atrial Appendage Occlusion Device Placement. Semin. Cardiothorac. Vasc. Anesth. 23, 248–255. https://doi.org/10.1177/1089253218758463

Vermeulen, B.D., Siersema, P.D., 2018. Esophageal Stenting in Clinical Practice: an Overview. Curr. Treat. Options Gastroenterol. 16, 260–273. https://doi.org/10.1007/s11938-018-0181-3

Watson, T., Webster, M.W.I., Ormiston, J.A., Ruygrok, P.N., Stewart, J.T., 2017. Long and short of optimal stent design. Open Hear. 4. https://doi.org/10.1136/openhrt-2017-000680

White, D.C., Elder, M., Mohamad, T., Kaki, A., Schreiber, T.L., 2016. Endovascular

Interventional Cardiology: 2015 In Review. J. Interv. Cardiol. 29, 5–10. https://doi.org/10.1111/joic.12273

Yang, M.C., Wu, J.R., 2018. Recent review of transcatheter closure of atrial septal defect. Kaohsiung J. Med. Sci. 34, 363–369. https://doi.org/10.1016/j.kjms.2018.05.001

Zaccaria, A., Migliavacca, F., Contassot, D., Heim, F., Chakfe, N., Pennati, G., Petrini, L., 2020a. Finite Element Simulations of the ID Venous System to Treat Venous Compression Disorders : From Model Validation to Realistic Implant Prediction. Ann. Biomed. Eng. https://doi.org/10.1007/s10439-020-02694-8

Zaccaria, A., Migliavacca, F., Pennati, G., Petrini, L., 2020b. Modeling of braided stents: Comparison of geometry reconstruction and contact strategies. J. Biomech. 107, 109841. https://doi.org/10.1016/j.jbiomech.2020.109841